# Analysis and control of vapor bubble growth inside solid-state nanopores

Soumyadeep PAUL*, Wei-Lun HSU*, Mirco MAGNINI**, Lachlan R. MASON****, Yusuke ITO*,
Ya-Lun HO*, Omar K. MATAR*** and Hirofumi DAIGUJI*

*Department of Mechanical Engineering, The University of Tokyo
7-3-1, Hongo, Bunkyo-ku, Tokyo 113-8656, Japan
E-mail: daiguji@thml.t.u-tokyo.ac.jp
**Department of Mechanical Engineering, University of Nottingham
NG7 2RD, Nottingham, United Kingdom
***Department of Chemical Engineering, Imperial College London
SW7 2AZ, London, United Kingdom
****The Alan Turing Institute, British Library
96 Euston Road, NW1 2DB London, United Kingdom

## Abstract

The increasing demands of computational power have accelerated the development of 3D circuits in the semiconductor industry. To resolve the accompanying thermal issues, two-phase microchannel heat exchangers using have emerged as one of the promising solutions for cooling purposes. However, the direct boiling in microchannels and rapid bubble growth give rise to highly unstable heat flux on the channel walls. In this regard, it is hence desired to control the supply of vapor bubbles for the elimination of the instability. In this research, we investigate a controllable bubble generation technique, which is capable of periodically producing bubble seeds at the sub-micron scale. These nanobubbles were generated in a solid-state nanopore filled with a highly concentrated electrolyte solution. As an external electric field was applied, the localized Joule heating inside the nanopore initiated the homogeneous bubble nucleation. The bubble dynamics was analyzed by measuring the ionic current variation through the nanopore during the bubble nucleation and growth. Meanwhile, we theoretically examined the bubble growth and collapse inside the nanopore by a moving boundary model. In both approaches, we demonstrated that by altering the pore size, the available sensible heat for the bubble growth can be manipulated, thereby offering the controllability of the bubble size. This unique characteristic renders nanopores suitable as a nanobubble emitter for microchannel heat exchangers, paving the way for the next generation microelectronic cooling applications.

*Keywords* : Joule heating, Nanopore, Bubble nucleation, Moving boundary problem, Microelectronic cooling

## 1. Introduction

With the advent of 3D stacked chips, the heat load per unit volume has significantly increased, requiring a more powerful and reliable cooling system. Therefore, in recent years, the development of highly efficient heat removal methods has become one of the critical issues in the global electronics industry. Due to their large heat capacity, two-phase microchannel heat sinks are regarded as a promising solution. In these devices, the refrigerant flows through the microchannels in contact with electronic chips and is then evaporated during the heat transfer from the walls. In comparison with single-phase cooling systems, the heat transfer using two-phase boiling is expected to be more efficient due to the remarkable latent heat consumed during the phase change. However, controlling vapor bubble generation on the microchannel surface can be a challenging task. Especially, under the conditions of high heat flux, vapor bubbles

generated from the wall surface has a potential to clog the channel (Prajapati and Bhandari, 2017). Eventually, the stuck and elongated bubbles may yield significant heat transfer reduction up to more than 50% (Yun, et al., 2005) and premature critical heat flux, ending up with high microchannel surface temperature. In the worst situation, the chip could be permanently damaged.

The severe channel dry-out can originate from the i) back flow of vapor bubbles due to the non-uniform heating of the chip architecture and ii) rapid bubble growth stemming from the high superheat needed at nucleation. To suppress the back flow of vapor bubbles, inlet restrictions placed at the entrance of the channel have been proved to be effective without a large additional pressure drop (Falsetti, et al., 2017; Szczukiewicz, et al., 2013). On the other hand, research studies have shown that possibility of the rapid bubble growth could be reduced by re-entrant cavities which lower the required superheat (Kuo and Peles, 2008; Kandlikar, et al., 2013). However, complicated microfabrication on microchannel surfaces can not only yield a high cost but also increase the pressure drop in the channels (Yin, et al., 2019). A more direct approach to decrease the bubble growth instability is to avoid the bubble nucleation on the microchannel walls. Thome and Dupont (2007) conceptualized this idea by proposing a nucleation chamber at the inlet of microchannel. A Pt wire inside the chamber produced tiny bubble seeds through Joule heating effects. The bubbles then flowed with the refrigerant into the microchannel for enhanced heat transfer. In a separate study, Xu et al. (2009) showed that the external bubble seeds (~10 μm) supplied at frequencies higher than 100 Hz may remarkably suppress the flow instability. In addition, by avoiding the stochastic nature of heterogeneous bubble nucleation on the wall surfaces, this scenario of external bubble seed supply facilitates the formation of a well-organized succession of bubbly, slug and annular flow patterns, enhancing the two-phase flow control. Moreover, barely no additional pressure drop was generated by the bubble seeds.
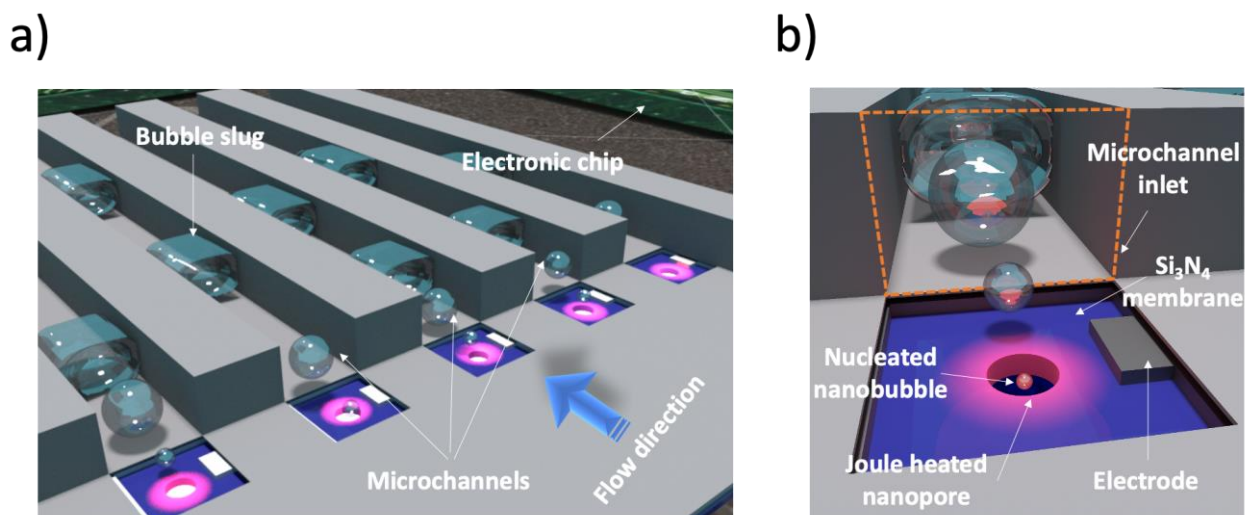


Fig. 1 a) Proposed operation of the nanopore bubble generator enabled microchannel heat sink. b) Close-up of nanopore bubble emitter at the microchannel inlet.

Adopting this concept, we herein propose a novel bubble seed generator for high performance microchannel heat exchangers. Instead of using wire heaters, we suggest a nanopore-based bubble emitter comprising of nanopores on a thin dielectric membrane placed at the inlets of microchannels (Fig. 1). Bubbles generated inside the nanopore by Joule heating are directly supplied to the microchannels where they grow and cool down the system. Bubble nucleation using nanopores was first proposed by Golovchenko and coworkers (Nagashima, et al., 2014; Levine, et al., 2016). They applied a high voltage (8.22 volts) across a small nanopore (107 nm) immersed in a 3M NaCl aqueous solution to produce Joule heat, resulting in localized superheating effects (the temperature at the pore centre reached around 600 K). Until the kinetic limit for homogeneous nucleation for pure water was surpassed, the nucleation of homogeneous bubbles from pore centre started occurring. The key features of this kind of bubble generation are:

I.    Uniform bubbles are generated quasi-periodically, largely alleviating stochasticity of the bubble nucleation.

II.    Homogeneous bubble nucleation can be achieved, making them easier to be driven into the microchannels.

III.    Aqueous solutions can be used as a refrigerant for 3D chips cooling.

Note that efficient and safe operation of 3D chips require heat flux removal rates as high as 1000 $W/cm^2$ while maintaining the chip under the 85 °C cutoff limit for safe operation. Previous studies have demonstrated heat transfer rates of 200-300 $W/cm^2$ using fluorocarbon refrigerants, keeping the chip temperatures within the safe limit (Madhour, et al., 2011). However, others have shown that two-phase cooling using fluorocarbon refrigerants is not always superior to single-phase water cooling especially at high mass flux rates (Park et al. 2019). At high flow rates the convective heat transfer of water could supersede the boiling heat transfer of fluorocarbon refrigerants due to the high inherent thermal conductivity of water. Additionally, despite the fact that they have been largely engineered to reduce their impact upon the ozone layer depletion, many of these fluorocarbon refrigerants still have a high global warming potential (Green, et al., 2015).

Considering its eco-friendly nature, high thermal conductivity and latent heat capacity, water has been regarded as an ideal refrigerant for high heat flux removal from 3D chips (Kandlikar, et al., 2011). However, due to its high saturation temperature, flow boiling using water poses two additional challenges: i) a higher operating temperature is needed increasing the overheating risk to chips, that the precise management of both temperature and pressure might be essential (Kosar, et al., 2005). ii) Heterogeneous bubble nucleation on the microchannel surface could give rise to rapid bubble growth due to high boiling incipience superheat. This issue might be resolved by using a nanopore nucleation chamber for seed bubble supply. A nano superheat hotspot can be created inside the nanopore through Joule heating while the rest of the microchannel remains at saturation conditions. Homogeneous bubble nucleation would be localized inside the nanopores and thus the high boiling incipience can barely affect the flow in the microchannels. It is expected that due to the limited amount of sensible heat around the nanopore, the bubble growth rate can be lower than the methods relying on heterogeneous nucleation. Compared to conventional bubble generation techniques such as wire heating or microheaters, nanopore, Joule heating provides focused heating and localized temperature distribution, making the bubble growth more controllable (Paul, et al., 2019). Note that, apart from its high saturation temperature, water being a non-dielectric refrigerant may pose a leakage risk. Kandlikar and Bapat (2007) pointed out that to meet the high heat dissipation requirements, leakage issues might need to be further examined for water. Recent research has emphasized on the design of leak free enclosures for fluid flow through microchannels (Dang, et al., 2016).

In this study, we investigate the bubble nucleation and dynamics in nanopores. We anticipate this type of bubble generation will be particularly suited for controlling boiling in microchannels with small hydraulic diameters, where bubble seeds of a few microns can be efficiently supplied. It should be noted that although we adopted highly concentrated electrolyte solutions in this work, for practical applications a lower salinity concentration could be sufficient to generate required Joule heat for homogeneous nucleation due to a higher surrounding temperature, avoiding potential salt residue caused by the evaporation of water in highly concentrated salt solutions.

## 2. Experimental
## 2.1 Nanopore fabrication

Nanopores were made on a silicon nitride chip (Alliance Biosystems Inc.), comprised of a 100 nm thick silicon nitride membrane deposited on a 200 μm thick silicon chip with a 50 μm × 50 μm square opening window at its centre. A through circular hole was etched at the centre of this window using a Ga+ Focused Ion Beam (FIB) machine (SMI3050: SII Nanotechnology). The chip was then sandwiched between two fluidic tanks (Fig. 2b) which were additively manufactured using a high-resolution 3D printer. In this configuration, the nanopore on the chip was the only channel connecting the two tanks. Two different sizes of the pore diameter ($D_p$ = 280 nm and $D_p$ = 525 nm) were fabricated. Scanning electron microscope (SEM) images of the nanopores are shown in Fig. 2a.

## 2.2 Nanopore voltammetry

The fluidic tank-chip assembly was filled with a 3M aqueous NaCl solution and high pulse voltages were applied by inserting Ag/AgCl electrodes to both solution tanks (Fig. 2c). The ionic current through the nanopore was obtained

from the shunt voltage across a shunt resistor connected in series with the pulse generator (Tektronix AFG3151C). At low voltages, there was only superheating in the pore evidenced by the increased pore conductance. Beyond a voltage threshold, the bubble nucleation started resulting in current blockage signals. A 500 MHz bandwidth oscilloscope
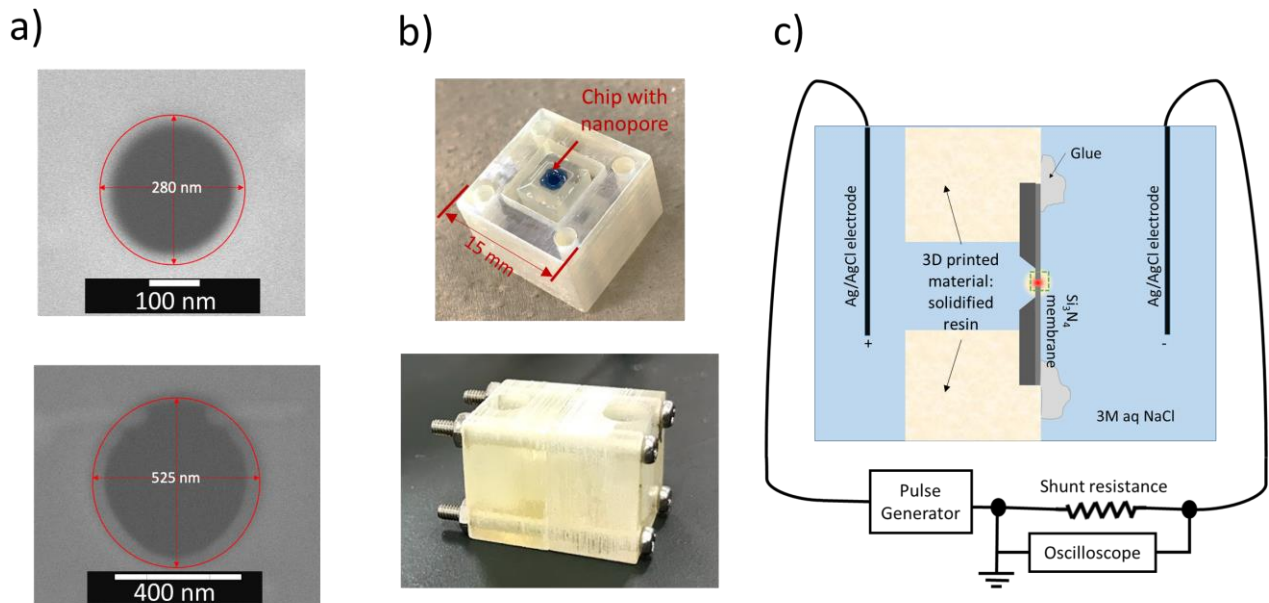


(Tektronix MDO3052) was used to measure the dip in shunt voltage as the nucleated bubble blocked ionic transport through the nanopore.

Fig. 2 a) SEM images of fabricated nanopores of diameters 280 nm (top) and 525 nm (bottom). b) Images of a nanopore chip glued to a 3D printed fluidic tank (top) and the assembled fluidic tank setup (bottom) c) Schematic of the nanopore voltammetry.

## 3. Modelling
### 3.1 Joule heating effects

Joule heating in electrolyte solutions when an electric field presents arises from the conductive ion transport behavior. Due to the remarkable cross-sectional area difference between the solution tank and the nanopore, the electric potential drop is focused in the nanopore resulting in localized Joule heating effects. Mathematically, the specific Joule heating rate, $H = \boldsymbol{J} \cdot \boldsymbol{E}$, where $\boldsymbol{E}$ is the electric field and $\boldsymbol{J} = \sigma\boldsymbol{E}$ is the ion flux, where $\sigma$ is the ionic conductivity. The ionic current through the nanopore is subject to two types of resistance: i) the access resistance which exists near the nanopore inlet and outlet and ii) the internal pore resistance (Gadaleta, et al., 2014). Considering a nanopore circuit model, the average electric field magnitude in the axial direction of the nanopore can be expressed as:

$$E_{\mathrm{p}} = \frac{V_{\mathrm{app}}}{L + \frac{\pi}{4}D_{\mathrm{p}}} \tag{1}$$

where $L = 100$ nm is the length of the nanopore equivalent to the thickness of the membrane and $V_{\mathrm{app}}$ denotes the bias voltage applied through the Ag/AgCl electrodes. As $V_{\mathrm{app}} = 7$ V, the specific Joule heating rates inside the nanopores ($H = \sigma E_{\mathrm{p}}^2$) reached $9.6 \times 10^{15}$ W/m$^3$ and $3.7 \times 10^{15}$ W/m$^3$ for the 280 nm and 525 nm pores, respectively ($\sigma = 20$ S/m). In the case, when the thermal diffusion is negligible, the corresponding temperature rise rates are estimated to be 2.3 K/ns and 0.9 K/ns ($\Delta T / \Delta t \approx H/\rho c_p$ where the liquid density, $\rho = 1000$ kg/m$^3$ and specific heat capacity, $c_p = 4200$ J/(kg·K). Note that as the thermal diffusion could play an important role in practice, the actual temperature rise would slightly slower). As the heating rate is the nanosecond scale which is much higher than the phonon relaxation times (in

the order of 1 ps), we neglect non-Fourier effects and employ the classical heat diffusion theory in the following analysis (Weeber, et al., 2013; Chen, et al., 2012).
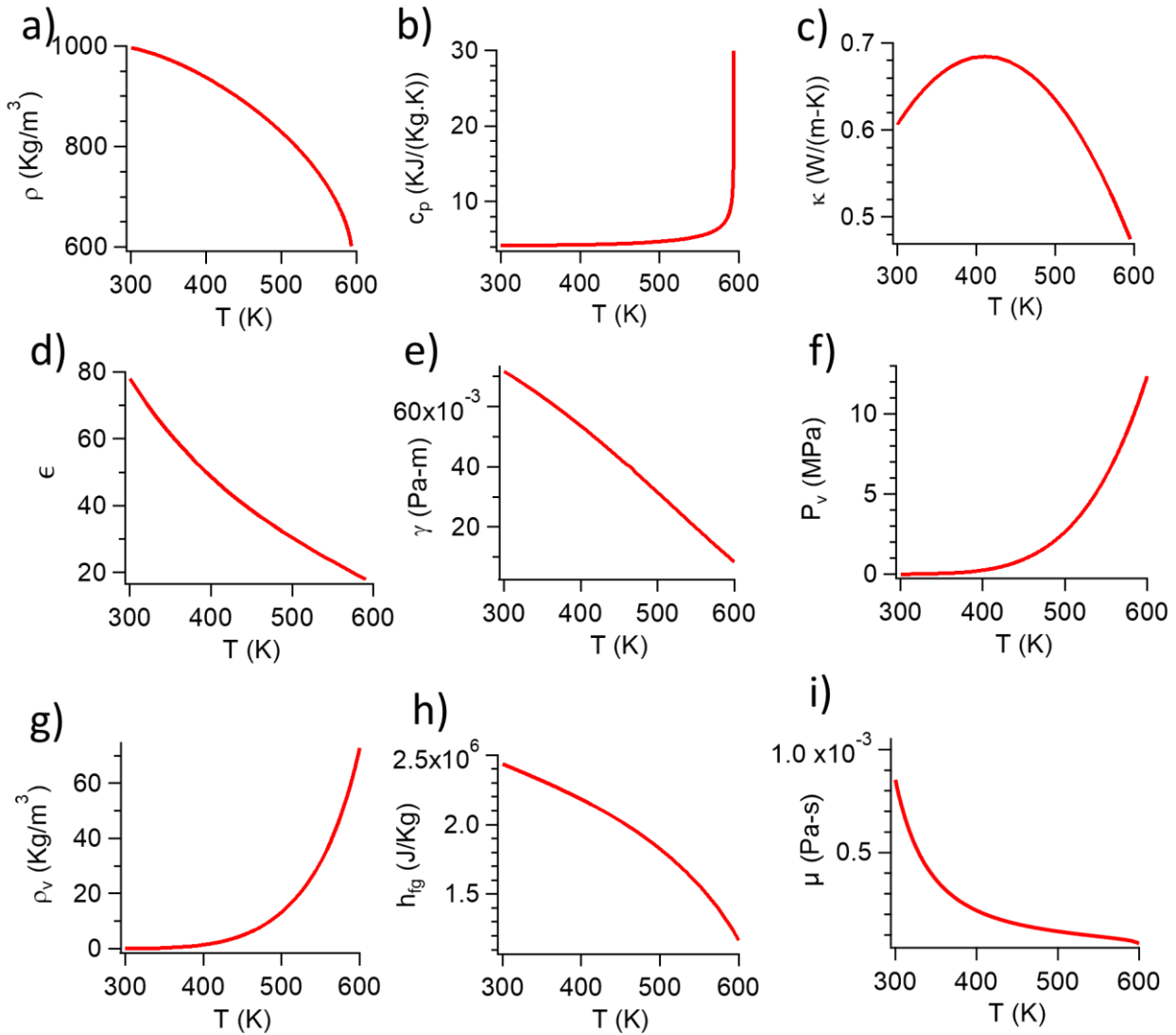


Fig. 3 Variations of a) liquid density, b) specific heat capacity, c) thermal conductivity, d) dielectric constant, e) surface tension, f) saturation vapor pressure, g) saturation vapor density, h) latent heat capacity and i) dynamic viscosity of water with temperature.

In the presence of thermal diffusion effects and the Joule heat source term, $H$, the energy balance of the electrolyte can be expressed as:

$$\rho c_p \frac{\partial}{\partial t}(T) = \nabla \cdot [k \nabla T] + \boldsymbol{J} \cdot \boldsymbol{E} \tag{2}$$

Here, the electrolyte properties including the specific heat $c_p$, thermal conductivity $k$ and density $\rho$ are modelled as functions of temperature, $T$ following a previous study (Levine, et al., 2016). The variations of the thermophysical properties of water with temperature are summarized in Fig. 3. Note that these relations were experimentally obtained at equilibrium, the fast increase of temperature might bring additional effects on these properties. The variations of these parameters are governed by the potential energy of water molecules, which depends on the water dipole moment and

hydrogen bond network structures, where the latter plays a key role in phase change processes. Although the initial heating rate can reach up to 1 K/ns, it is still considerably slower than the relaxation time of hydrogen bond rearrangement in water, which is around 1-10 ps (Ohmine and Saito, 1999). Therefore, we consider the relations remain robust during the heating process.

On the other hand, the conservation of energy for the silicon nitride membrane can be expressed as:

$$\rho_{\text{SiNx}} c_{p\text{SiNx}} \frac{\partial}{\partial t}(T) = k_{\text{SiNx}} \nabla^2 T \qquad (3)$$

where $\rho_{\text{SiNx}} = 3100$ kg/m$^3$, $c_{p\text{SiNx}} = 700$ J/(kg·K), $k_{\text{SiNx}} = 3.2$ W/(m·K) are the density, specific heat and thermal conductivity of silicon nitride, respectively (Levine, et al., 2016). The charge conservation can be modelled as:

$$\nabla \cdot \boldsymbol{J} + \frac{\partial \rho_{\text{e}}}{\partial t} = 0 \qquad (4)$$

where $\rho_e = \nabla \cdot [\epsilon(T)\epsilon_0 \boldsymbol{E}]$ is the space charge density and $\epsilon$ is the dielectric constant of water as a function of temperature (Levine, et al., 2016) while $\epsilon_0$ is the dielectric permittivity of free space. As Joule heating begins, the pore temperature starts rising, increasing the ionic conductivity as $\sigma(T) = mT - b - ((T - 293.15)^{\alpha})/\beta$ , where the parameters $m$, $b$ and $\beta$ are 0.391 S/(m·K), 96.9 S/m and 5.6×10$^4$ respectively (Levine, et al., 2016). $\alpha$ is a fitting parameter = 2.53 and 2.5 for the cases of 7.08 V for 525 nm pore and 7.06 V for 280 nm pore, respectively (as summarized in Table 1). As the simulation current magnitudes match the experimental measurements, we output the theoretical temperature distributions in the nanopores (Paul, et al., 2019).

Table 1   Simulation conditions for the two pore sizes

| Case | Pore diameter, $D_{\text{p}}$ [nm] | Bias voltage, $V_{\text{app}}$ [V] | Joule heating parameter, $\alpha$ | Room temperature, $T_0$ [K] |
|---|---|---|---|---|
| (i) | 280 | 7.06 | 2.5 | 296.55 |
| (ii) | 525 | 7.08 | 2.53 | 300.15 |

We simulate Joule heating in the 2D cylindrical co-ordinates (*y*, *z*) as shown in Fig. 4a, where *y* denotes the radial direction and *z* the axial direction. The domain extends for 75 μm from the pore centreline to the top edges and 150 μm from the inlet to outlet edges. We apply a symmetry condition to the temperature and no ionic flux in the radial direction on the pore centreline. On the silicon nitride walls are considered as ion impermeable and zero ionic flux is applied to the top boundaries, ($J_{\text{n}} = \boldsymbol{J} \cdot \hat{n} = 0$). We assume the temperature and heat flux are continuous at the solution-Si$_3$N$_4$ interface. For the boundary edges of the nanopore system, the temperature is fixed at room temperature. On the other hand, an electric potential difference is applied between the inlet and outlet. As shown in Fig. 4b, c, a structured mesh is adopted within the nanopore and on the pore surface while the rest of the solution domain is discretized using an unstructured mesh. The entire Si$_3$N$_4$ membrane is discretized using a finely structured mesh. Inside the nanopore area, the mesh sizes are in the order of a few nanometres. We first solved the steady state electric potential independently as $\nabla \cdot \boldsymbol{J} = 0$ subject to the ion flux boundary conditions. Then, the result of this simulation is used as the initial conditions for the transient Joule heating simulations described by Eqs. (2)-(4). The time step, Δt was designed to gradually increase from 10 fs to capture the rapid temperature variation at the beginning stage:

$$\Delta t = 10^{-(7\exp(-0.005(n-1))+7)} \qquad\qquad (5)$$

Here $n$ denotes the number of the time step. The present boundary condition problem is implemented and solved using a numerical package, arb (Harvie, 2010), based on an implicit finite volume method.
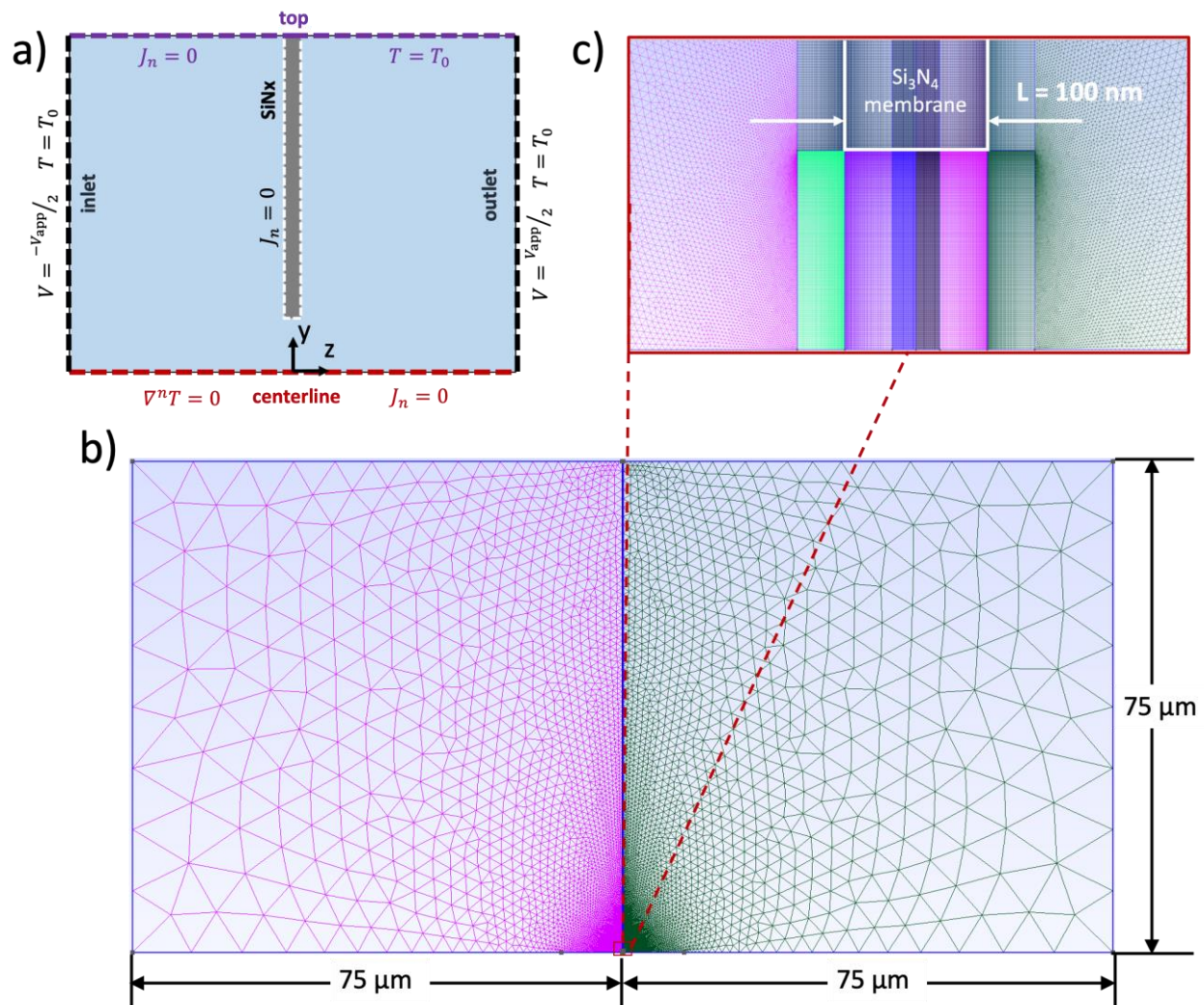


Fig. 4 a) Boundary conditions used for the Joule heating simulation, where $V_{app}$ is the applied bias voltage, $T_0$ is the room temperature and $J_n$ is the ion flux normal to the boundary. b) A 2D mesh of the nanopore system for the $D_p = 280$ nm pore with a typical number of 314316 cells. c) The structured mesh inside and around the nanopore.

## 3.2 Bubble growth in a superheated liquid

The classical bubble growth procedure (Prosperetti, 2018; Prosperetti and Plesset, 1978) has been well described for infinite superheated liquids where the growth process can be divided into three stages: i) the inertial growth after the nucleation due to the disruption of Laplace equilibrium and ii) the thermal growth stage where the evaporation at the interface is dominant and iii) the diffusive growth where the dissolved gas in the liquid starts filling the bubble. In contrast, the nanopore bubble growth follows a different route particularly because of the sharp temperature gradient in the nanopore. Due to the focused Joule heating, the amount of sensible heat inside the nanopore is limited, although close to 600 K is reached at the pore centre. At this temperature, a nanometer sized vapor nucleus is formed with vapor pressure reaching 12 MPa. Due to this high vapor pressure, there exists a tremendous acceleration of the bubble growth in the radial direction just after the formation of critical nucleus leading to a high inertial growth velocity. However, due to lack of sufficient sensible heat in liquid, the condensation sets in at the bubble interface much before the end of the inertial growth, triggering bubble collapse. As shown in Fig. 5, when the bubble nucleus grows, a thermal boundary layer is formed at the interface and the liquid temperature decreases radially from a peak value of $T_p$ to the room temperature $T_0$. A similar temperature distribution was

previously reported by Okuyama et al. (2006) when studying the bubble growth on a rapidly heated film immersed in ethyl alcohol. Soon after the nucleation, the bubble expands and the vapor temperature, $T_v$ decreases from the nucleation temperature, $T_{nuc}$ causing a positive temperature gradient at the interface ($dT/dr|_{interface} > 0$, where $r$ represents the radial distance from the bubble centre). This results in a net heat flux, $q_r$ driving the bubble growth via the evaporation at the interface. As the bubble grows, $T_p$ decreases rapidly because of i) the loss of the heat source for the evaporation, ii) the diffusive cooling due to the radial heat flux, $q_d$ to the bulk liquid. The temperature distribution directly affects the rate of diffusive cooling according to Fourier's law. In other words, a localized temperature distribution will lead to a fast decrease of $T_p$. Consequently, $q_r$ decreases slowing down the bubble growth. Indeed, this deceleration of the bubble growth can benefit the control of bubble seed generation for two-phase microchannel heat sinks. As the temperature at the thermal boundary layer, $T_p$ changes with time, the traditional bubble growth model based on a constant liquid temperature becomes invalid (Prosperetti, 2018; Prosperetti and Plesset, 1978). Thus, we conduct numerical simulations to examine the bubble growth inside the nanopore.
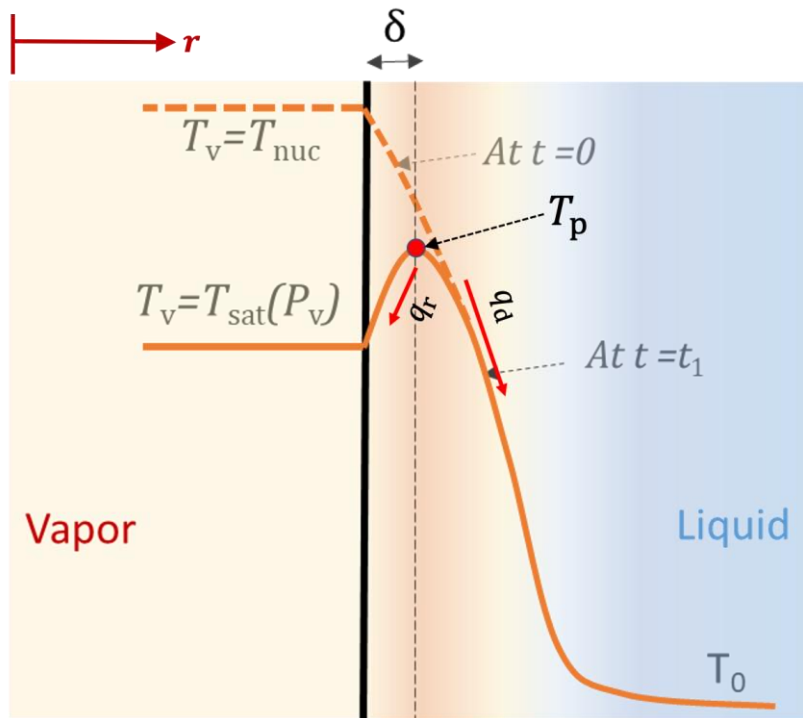


Fig. 5 Temperature distribution during the initial growth phase of hotspot boiling.

In the numerical model, we assume the bubble growth to be spherically symmetric while the bubble centre remains stationary at the pore centre. Without mass generation in the liquid, the continuity equation of the liquid can be expressed as:

$$\frac{\partial \rho}{\partial t} + \frac{1}{r^2}\frac{\partial}{\partial r}(r^2 \rho u) \approx \frac{1}{r^2}\frac{\partial}{\partial r}(r^2 \rho u) = 0 \tag{6}$$

The equation can be further simplified to $F(t) = r^2 \rho(r) u(r,t) = R^2 \rho(R)\dot{R}$, where $F(t)$ is the radial outflow of water as the bubble grows, $\rho(r)$ is the liquid density and $u(r,t)$ is the radial velocity of liquid. $R$ represents the radius of the bubble at any given time point. The momentum balance of the liquid in the radial direction can be derived as:

$$\rho \frac{Du}{Dt} = \rho\left(\frac{\partial u}{\partial t} + u\frac{\partial u}{\partial r}\right) = -\frac{\partial P}{\partial r} + 2\left[\frac{1}{r^2}\frac{\partial}{\partial r}\left(\mu r^2 \frac{\partial u}{\partial r}\right) - \frac{2\mu u}{r^2}\right] \tag{7}$$

$\mu$ and $P$ represent the liquid viscosity and pressure. After substituting $u$ with $F$, we obtain:

$$\frac{\dot{F}}{r^2} - \frac{F^2}{r^5}\left(\frac{\rho' r}{\rho^2} + \frac{2}{\rho}\right) = -\frac{\partial P}{\partial r} - \frac{2F}{r^2}\left[\left(\frac{\rho'}{\rho} + \frac{2}{r}\right)\frac{\partial}{\partial r}\left(\frac{\mu}{\rho}\right) + \frac{\mu}{\rho}\frac{\partial}{\partial r}\left(\frac{\rho'}{\rho}\right)\right] \tag{8}$$

where $\rho' = \frac{\partial \rho}{\partial r}$ and $\mu' = \frac{\partial \mu}{\partial r}$ denote the spatial derivative of liquid density and viscosity, respectively. $F$ and $\dot{F} = \frac{dF}{dt}$ are functions of time only. In this regard, for each time step, Eq. (8) can be integrated with respect to $r$ from $R$ to $R_\infty$ to obtain the liquid pressure at the interface, $P_i$.

$$P_i - P_\infty = \dot{F} \int_R^{R_\infty} \frac{dr}{r^2} - F^2 \int_R^{R_\infty} \left[ \frac{(\rho' r + 4\rho)}{\rho^2 r^5} - \frac{2}{\rho r^5} \right] dr + 2F \int_R^{R_\infty} \left[ \frac{\mu}{\rho^2 r^2} \left( \rho'' - \frac{2\rho'^2}{\rho} - \frac{2\rho'}{r} \right) + \frac{\mu'}{\rho r^2} \left( \frac{2}{r} + \frac{\rho'}{\rho} \right) \right] dr \qquad (9)$$

$$P_i - P_\infty = \left( \rho R^2 \ddot{R} + 2\rho R \dot{R}^2 \right) \left( \frac{1}{R} - \frac{1}{R_\infty} \right) - \rho^2 R^4 \dot{R}^2 \left( \frac{1}{\rho(R) R^4} - \frac{1}{\rho(R_\infty) R_\infty^4} \right) + \rho^2 R^4 \dot{R}^2 \int_R^{R_\infty} \frac{2}{\rho r^5} dr +$$

$$\rho R^2 \dot{R} \int_R^{R_\infty} 2 \left[ \frac{\mu}{\rho^2 r^2} \left( \rho'' - \frac{2\rho'^2}{\rho} - \frac{2\rho'}{r} \right) + \frac{\mu'}{\rho r^2} \left( \frac{2}{r} + \frac{\rho'}{\rho} \right) \right] dr \qquad (10)$$

Equation (10) is numerically solved over $10^5$ uniformly distributed points ranging from $R$ to $R_\infty$ for each time step. $R_\infty$ is chosen to be sufficiently far away from the pore centre where the liquid temperature approaches room temperature, i.e. $T = T_0$ and liquid pressure approaches atmospheric pressure, $P_\infty$ i.e. $P = P_\infty$. Using the force balance at the interface (Brennen, 2003; Nikolayev and Beysens, 1999), we obtain the following equation:

$$P_v - P_i - \frac{4\mu}{R} \dot{R} - 2\frac{\gamma}{R} = -\dot{m} |\dot{m}| \left( \frac{1}{\rho_v(T_v)} - \frac{1}{\rho(T_v)} \right) \qquad (11)$$

Here $P_v$ and $\rho_v$ are the pressure and density inside the bubble considered to be equal to the saturation vapor pressure and saturation vapor density. They vary with the saturation temperature according to Wagner and Pruß (2002). $\gamma$ is the surface tension coefficient. $\gamma$ and $\mu$ were obtained as a function of the liquid temperature following the property-temperature relationships given by Haynes (2016) and Cooper and Dooley (2008) respectively. The term on the right hand side denotes the recoil force (Nikolayev and Beysens, 1999) experienced by the interface due to the difference between the momentum of vapor evaporating from the liquid side and the momentum entering the bubble side of the interface. $\dot{m}$ is the vapor influx at interface which can be obtained by considering the evaporation of water under the temperature gradient across the thermal boundary layer:

$$\dot{m} = \frac{\kappa \frac{dT}{dr}\big|_{interface}}{h_{fg}} \qquad (12)$$

where $h_{fg}$ is the saturation temperature dependent latent heat capacity following Haynes (2016). Combining Eqs. (10) and (11) we can express the bubble radius, $R$ in terms of the vapor pressure as follows:

$$P_v - P_\infty - \left( \rho R^2 \ddot{R} + 2\rho R \dot{R}^2 \right) \left( \frac{1}{R} - \frac{1}{R_\infty} \right) + \rho^2 R^4 \dot{R}^2 \left( \frac{1}{\rho(R) R^4} - \frac{1}{\rho(R_\infty) R_\infty^4} \right) - \rho^2 R^4 \dot{R}^2 \int_R^{R_\infty} \frac{2}{\rho r^5} dr -$$

$$\rho R^2 \dot{R} \int_R^{R_\infty} 2 \left[ \frac{\mu}{\rho^2 r^2} \left( \rho'' - \frac{2\rho'^2}{\rho} - \frac{2\rho'}{r} \right) + \frac{\mu'}{\rho r^2} \left( \frac{2}{r} + \frac{\rho'}{\rho} \right) \right] dr - \frac{4\mu}{R} \dot{R} - 2\frac{\gamma}{R} = -\dot{m} |\dot{m}| \left( \frac{1}{\rho_v(T_v)} - \frac{1}{\rho(T_v)} \right) \qquad (13)$$

$$P_v - P_\infty - \left( \rho R^2 \ddot{R} + 2\rho R \dot{R}^2 \right) A + \rho^2 R^4 \dot{R}^2 (B - C) - \rho R^2 \dot{R} D - \frac{4\mu}{R} \dot{R} - 2\frac{\gamma}{R} = E \qquad (14)$$

where $A = \left( \frac{1}{R} - \frac{1}{R_\infty} \right)$, $B = \left( \frac{1}{\rho(R) R^4} - \frac{1}{\rho(R_\infty) R_\infty^4} \right)$, $C = \int_R^{R_\infty} \frac{2}{\rho r^5} dr$, $D = \int_R^{R_\infty} 2 \left[ \frac{\mu}{\rho^2 r^2} \left( \rho'' - \frac{2\rho'^2}{\rho} - \frac{2\rho'}{r} \right) + \frac{\mu'}{\rho r^2} \left( \frac{2}{r} + \frac{\rho'}{\rho} \right) \right] dr$

and $E = -\dot{m} |\dot{m}| \left( \frac{1}{\rho_v(T_v)} - \frac{1}{\rho(T_v)} \right)$. When we assume constant liquid density and viscosity and no recoil force, this equation converges into the classical Rayleigh-Plesset equation.

$$R\ddot{R} + \frac{3}{2} \dot{R}^2 = \frac{1}{\rho} \left( P_v - P_\infty - 2\frac{\gamma}{R} - 4\frac{\mu}{R} \dot{R} \right) \qquad (15)$$

The mass flux can be expressed using the conservation of bubble mass, *viz*:

$$\dot{m} = \frac{1}{4\pi R^2} \frac{d}{dt}\left(\rho_v \frac{4\pi R^3}{3}\right) = \left(\rho_v \frac{dR}{dt} + \frac{R}{3}\frac{d\rho_v}{dt}\right) = \left(\rho_v \frac{dR}{dt} + \frac{R}{3}\frac{dT_v}{dt}\frac{d\rho_v}{dT_v}\right) \tag{16}$$

To derive the mass flux, $\dot{m}$ we acquire the temperature gradient at the interface via Eq. (12) by solving the energy conservation equation in the superheated liquid as:

$$\rho\frac{Dh}{Dt} = \rho c_p\left(\frac{\partial T}{\partial t} + u\frac{\partial T}{\partial r}\right) = \frac{1}{r^2}\left(\frac{\partial}{\partial r}\left(r^2 k\frac{\partial T}{\partial r}\right)\right) = k\left(\frac{2}{r}\frac{\partial T}{\partial r} + \frac{\partial^2 T}{\partial r^2}\right) + \frac{\partial T}{\partial r}\frac{\partial k}{\partial r} \tag{17}$$

where $h$ represents the specific enthalpy of liquid. A 1D moving boundary model in the radial direction proposed by Robinson and Judd (2004) is used to study the bubble growth behavior, starting from the critical nucleus at nucleation and the radius of which is given by:

$$R_c = \frac{2\gamma(T_{nuc})}{P_v(T_{nuc}) - P_\infty} \tag{18}$$

Here, the nucleation temperature, $T_{nuc}$ is equal to the temperature at the pore centre, $T_c$. At the moment of inception of the first bubble event $t_{nuc}$, a subtle perturbation of radius in the molecule level addition to the critical nucleus disturbs the Laplace equilibrium triggering the bubble growth. During the expansion, the temperature inside the bubble is assumed to be uniform and saturated. Equation (14) is discretized and solved by a 1D mesh as shown in Fig. 6a,b.
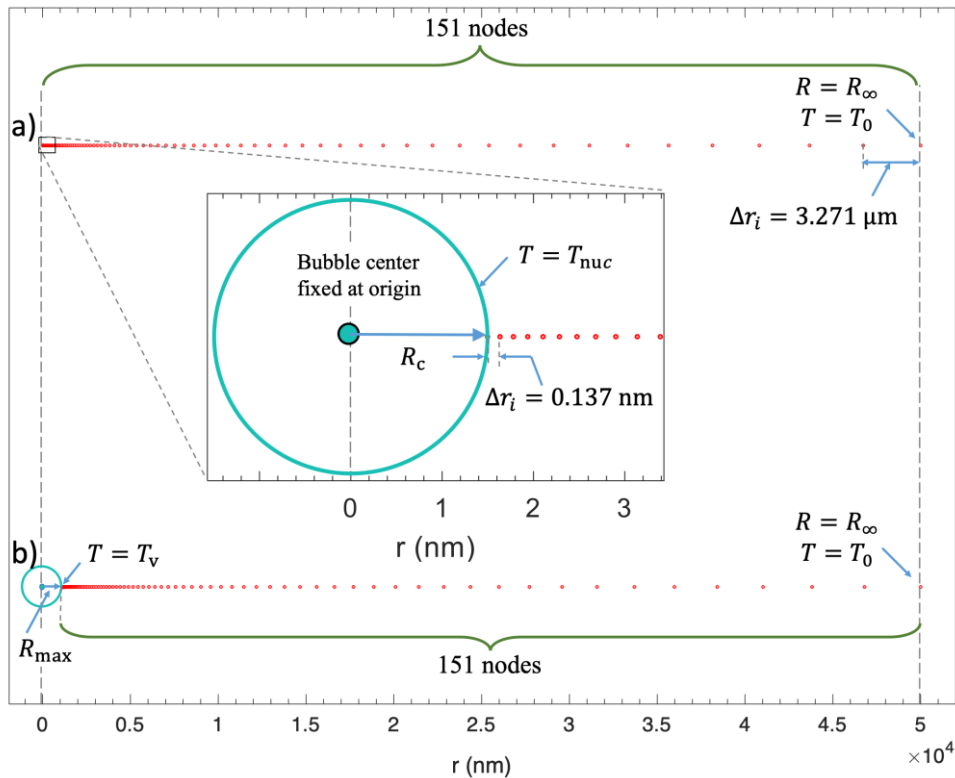


Fig. 6 a) 1D mesh discretization for bubble dynamics simulations at nucleation point. 151 computational nodes are distributed radially starting from the bubble surface to $r = 50$ μm from the bubble surface. The mesh size varies from $\Delta r_i = 0.137$ nm at the bubble interface to $\Delta r_i = 3.271$ μm at the other end. The temperature distribution in $z$ direction in Fig. 4a at nucleation point was used as initial condition for bubble dynamics simulation. b) Mesh gets compressed as the bubble grows from $R_c$ to $R_{max}$. In this figure, $R_{max}$ represents the maximum bubble radius attained during bubble growth inside the 280 nm nanopore.

Due to a higher temperature gradient, the computational nodes are closely distributed near the bubble surface whereas the distribution gradually becomes sparse towards the bulk. The positions of the 151 computational nodes follow a geometric progression below:

$$R_{\mathrm{CN}}(i) = R + \frac{(R_\infty - R)(\omega^{i-1} - 1)}{\omega^{N} - 1}, \text{ for } 1 \le i \le 150 \tag{19}$$

and $R_{\mathrm{CN}}(151) = R_\infty = 50$ μm, $\omega = 1.07$, $N = 150$ and $i$ is the index denoting the computational node. The position of computational nodes or 1D mesh grid can be seen in Fig. 6.

The temperature distribution in the $z$-direction inside the nanopore (Fig. 4a) at the nucleation point obtained from Joule heating simulations is used as an initial condition. At the nucleation point, a bubble of a critical radius was inserted at the centre of the nanopore ($r = 0$) and the temperature distribution is shifted in the $+r$ direction according to:

$$T_{t=0}(r) = T_{t=0}{}^* \left( r - R_\mathrm{c} \left( 1 - \left( \frac{\rho_\mathrm{v}(T_\mathrm{nuc})}{\rho(T_\mathrm{nuc})} \right)^{\frac{1}{3}} \right) \right) \tag{20}$$

Here we assume a sphere volume of liquid at the nucleation temperature evaporates and thus creating a spherical volume of vapor. As the vapor sphere has a larger volume than the evaporating liquid sphere, the temperature distribution starting from the liquid sphere surface is estimated by the offset amount to obtain the radial temperature distribution from the bubble surface (at superheat temperatures ~ 598 K, the ratio of $\rho_\mathrm{v}/\rho = 0.1487$ and thus cannot be neglected). $T_{t=0}$ is the temperature distribution after the shifting and $T_{t=0}{}^*$ is the temperature distribution inside the nanopore along the $+z$ direction.

Transient bubble growth behavior is solved in MATLAB. For each time step, Eq. (17) is solved to update the temperature. We transform Eq. (17) from a moving mesh onto a stationary grid of 151 points with unit grid spacing (Robinson and Judd, 2004) through spatial metrices, $r_i = \frac{\partial R_{\mathrm{CN}}}{\partial i}$, $r_{ii} = \frac{\partial^2 R_{\mathrm{CN}}}{\partial i^2}$, $k_i = \frac{\partial k}{\partial i}$ ($i$ represents the index of computational node) and temporal metric, $r_\tau = \frac{\partial R_{\mathrm{CN}}}{\partial t}$ ($\tau = t$), so that it can be solved using traditional finite difference methods.

$$T_\tau + a T_i + b T_{ii} = 0 \tag{21}$$

where $T_\tau = \frac{\partial T}{\partial t} + r_\tau \frac{\partial T}{\partial r}$, $T_i = \frac{\partial T}{\partial i}$, $T_{ii} = \frac{\partial^2 T}{\partial i^2}$, $a = \frac{u(i) - r_\tau}{r_i} - \frac{k}{\rho c_p} \left( \frac{2}{r_i R_{\mathrm{CN}}(i)} - \frac{r_{ii}}{r_i^3} \right) - \frac{k_i}{\rho c_p} \frac{1}{r_i^2}$ and $b = -\frac{k}{\rho c_p} \frac{1}{r_i^2}$. All single and double partial spatial derivatives in Eq. (21) are expressed as second order finite differences. The temperature dependent thermo-physical properties are calculated at temperatures from the previous time step. We used the Dirichlet boundary conditions $T = T_\mathrm{v}$ at the bubble interface and $T = T_0$ at the other end of the 1D mesh as shown in Fig. 6. From the updated temperature distribution, $dT/dr$ is calculated at the interface, which is used to derive the vapor influx, $\dot{m}$ using Eq. (12). Using the temperature distribution, the liquid density and viscosity are acquired at the 151 1D mesh nodes and then interpolated over a finer grid of $10^5$ points on which the two definite integrals in Eq. (14), $C$ and $D$ are calculated. Eq. (14) and (16) are solved simultaneously using the 4th order Runge-Kutta method to obtain the bubble radius $R$, growth rate $\dot{R}$ and vapor temperature $T_\mathrm{v}$. During the Runge-Kutta steps the terms $A$, $B$, $C$, $D$ and $E$ are evaluated at the previous time step and kept constant while the vapor pressure, $P_\mathrm{v}$, liquid density, $\rho$, dynamic viscosity, $\mu$ and vapor density, $\rho_\mathrm{v}$ in the remaining terms are evaluated at $T_\mathrm{v}$. Using the updated value of $R$, the 1D grid is re-meshed using Eq. (19) and the grid transformation metrics for Eq. (21) are updated. Afterwards, Eq. (21) is solved to obtain the temperature distribution in the liquid for the next time step using the updated vapor temperature as a boundary condition at the bubble interface. The time difference is chosen for each time step such that at the interface i) the interface growth or shrink is less than or equal to 20% of the grid spacing and ii) the vapor evaporated or condensed at interface accounted for less than or equal to 20% of the grid spacing. Mathematically, it can be expressed as:

$$\Delta t_n = \min \left\{ 10^{-(3 \exp(-0.003n) + 11)}, 0.2 \frac{\Delta r_{interface}}{|dR/dt|_{n-1}}, 0.2 \frac{\rho \Delta r_{interface}}{|\dot{m}|_{n-1}} \right\} \tag{22}$$

Here $n$ denotes the index of the time steps. It should be noted that in the bubble dynamic simulations, we do not take the Joule heating source term in the energy equation, Eq. (17), into account. This term would exist only when the bubble is growing and partially blocking the pore during which the current flow persists. However, compared to the total blockage duration, the partial blockage time is much shorter due to the high velocity of bubble growth after the nucleation. Accordingly, the heat added during the partial blockage time should not contribute significantly to the overall bubble dynamics. In our simulations, the bubble growth or collapse is assumed to be spherically symmetric with only two phases, being the a) vapor extending from $r = 0$ to $r = R$ and ii) liquid from $r = R$ to $r = R_\infty$. The presence of the silicon nitride membrane is neglected and as a result the heat dissipation from the superheated liquid through the membrane is not considered.

## 4. Results and discussion

In the experiment, upon the application of a bias voltage across the nanopore, ion migration was triggered. Under a high electric field, the high ion flux gave rise to intense and localized Joule heat in the order of $10^{16}$ W/m³ inside the nanopore. In consequence, the temperature soared up yielding a superheating condition. As the silicon nitride has a higher thermal conductivity than water, the liquid temperature at the pore centre was higher than that near the walls, elevating the probability of homogeneous nucleation. According to classical nucleation theory (Debendetti, 1996; Levine, et al., 2016), the homogeneous nucleation rate, $I_{ho}$ as a function of liquid temperature is given by:

$$I_{ho}(T) = \frac{\rho}{M}\sqrt{\frac{3\gamma}{\pi M}}\exp\left[-\frac{W^*}{k_B T}\right] = \frac{\rho}{M}\sqrt{\frac{3\gamma}{\pi M}}\exp\left[-\frac{16\pi\gamma^3}{3k_B T\left(P_v - P_\infty\right)^2 \phi^2}\right] \tag{23}$$

where $M$ denotes the mass of a water molecule, $k_B$ is the Boltzmann constant and $\phi = 1 - \rho_v/\rho + 0.5(\rho_v/\rho)^2$. $I_{ho}$ represents the number of critically sized nuclei formed per unit time and per unit volume. From a thermodynamic viewpoint, as temperature of the liquid increases, the free energy barrier for nuclei formation, $W^*$ reduces allowing the possibility for local energy and density fluctuations to induce the formation of a new phase. From a kinetic viewpoint, as the liquid temperature increases, the population of critically sized nuclei rises. Thus $I_{ho}$ increases, thereby increasing the likelihood of nuclei formation. Figure 7a,b (inset) shows the contour plots of the temperature distribution in the nanopore at nucleation. The nucleation point, $t_{nuc}$ was observed from the experiments when a current blockage signal was observed (Fig. 8a,c). Figure 7c shows the variation of $I_{ho}$ along the axial direction of the pore (i.e., in the $z$-direction in Fig. 4a) corresponding to the temperature distribution at $t_{nuc}$. As expected, the nucleation rate was highest at the pore centre where the peak liquid temperature occurred. The probability of nucleation after time, $t$, $Q(t)$ can be expressed as (Asai, 1989):

$$\frac{dQ}{dt} = K(t)(1 - Q) \tag{24}$$

which is subject to the initial conditions of $Q = 0$, at $t = 0$. Here $K(t) = \iiint I_{ho}\,dV$ is the volume integral of homogeneous nucleation rate over the liquid region in the Joule heating simulations evaluated at each time step. This leads to the following equation for each time step:

$$Q_n = 1 - (1 - Q_{n-1})\exp(-K(t_{n-1})\Delta t_{n-1}) \tag{25}$$

The time variation of $Q$ is shown in Fig. 7d. It is found that for both pore sizes, there was a step-like rise in $Q$, indicating a strict cutoff for homogeneous nucleation. For the 525 nm and 280 nm pores, the cutoff temperatures are 591 K and 592 K, respectively. This is consistent with the experimental observations that there existed a long waiting time before the first homogeneous nucleation.
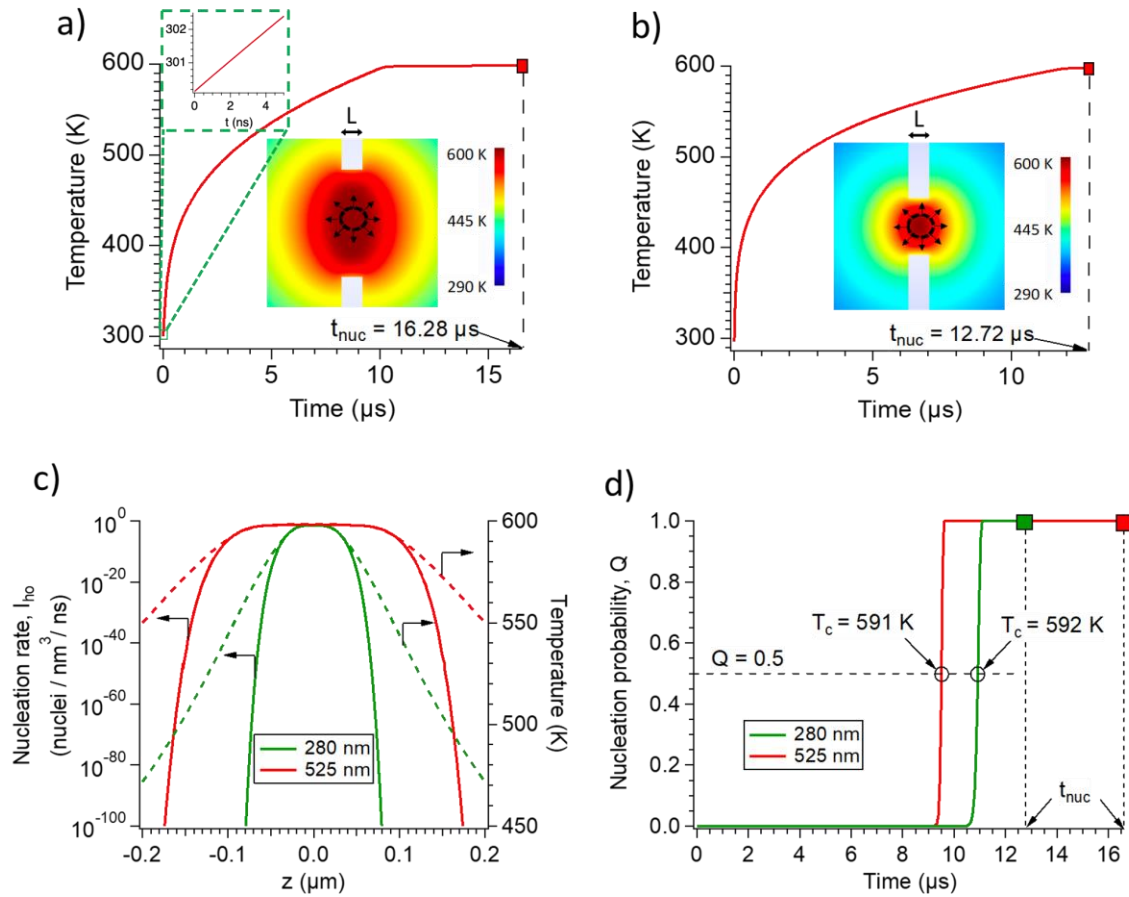
Fig. 7 Transient development of the liquid temperature at the pore centre, $T_c$ for a) Case i: $V_{app}$ = 7.08 V on $D_p$ = 525 nm pore and b) Case ii: $V_{app}$ = 7.06 V on $D_p$ = 280 nm pore). The contour plots in the inset indicate the spatial temperature distribution in the nanopore at the nucleation point, $t_{nuc}$. c) Variations of nucleation rate (solid lines) and liquid temperature (dotted lines) along the nanopore axis at $t_{nuc}$ for different pore sizes. d) Variation of nucleation probability with time for different pore sizes.

It should be noted that thermodynamic properties of pure water are used to perform the Joule heating simulations and estimate the nucleation rate. However, in the experiments, as a 3M aqueous solution was used, the presence of highly concentrated ions could affect the liquid density, permittivity, specific heat, surface tension and viscosity, where the precisely measured values are not available in the literature at metastable states to the best of our knowledge. Additionally, the local ion concentration varies in response to the temperature gradient (i.e. thermophoresis) posing additional uncertainties in these thermal properties. However, it is anticipated that the presence of ions would not affect the homogeneous nucleation temperature significantly. As shown in Fig. 7c that the magnitude of $I_{ho}$ changes sharply in response to a subtle temperature change, due to its exponential relationship with $W^*$. The order of magnitude of $I_{ho}$ is given by:

$$\log I_{ho} = \log \frac{\rho}{M}\sqrt{\frac{3\gamma}{\pi M}} - \frac{16\pi\gamma^3}{3k_B T\left(P_v - P_\infty\right)^2 \phi^2} = \log \frac{\rho}{M}\sqrt{\frac{3\gamma}{\pi M}} - G \tag{26}$$

The order of magnitude of $I_{ho}$ is sensitive to the variation of $G$, which varies significantly with $\gamma$ and $P_v$. The presence of ions in the solution will increase $\rho$ and $\gamma$. Ali and Bilal (2009) showed that $\gamma$ increases by 5-6% when the salinity concentration is increased from 0 M to 2 M for the temperature between 10 and 30 ℃. Accordingly, the error of $I_{ho}$ can be expressed as

$$-\frac{\Delta G}{G} = -\frac{3}{\gamma}\Delta\gamma \tag{27}$$

This indicates the order of magnitude error is in the range of 15-18% due to the presence of salt. On the other hand, the error in the solution temperature can be estimated by:

$$-\frac{\Delta G}{G} = -\frac{3}{\gamma}\Delta\gamma + \frac{2}{(P_v - P_\infty)}\Delta P_v + \frac{2}{\phi}\Delta\phi \tag{28}$$

According to Eq. (28), the temperature variation in the range of ~2-3 K would exist when the error of $G$ is at 15%, indicating that the presence of salt would not significantly affect the homogeneous nucleation temperature.
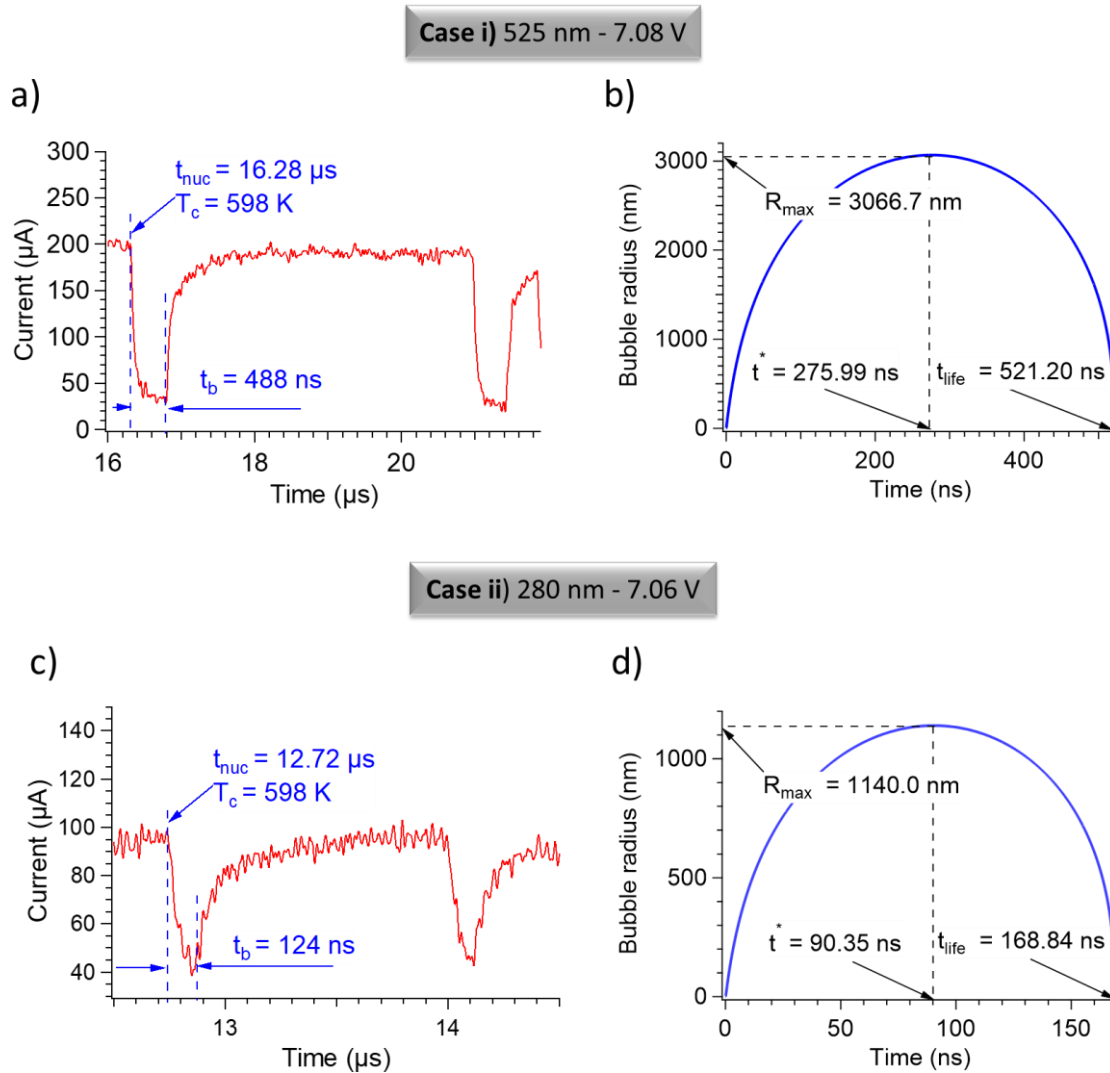


Fig. 8 a,c) Experimental current blockage signals due to the presence of bubbles for the two cases (Case i: $V_{app} = 7.08$ V at $D_p = 525$ nm and Case ii: $V_{app} = 7.06$ V at $D_p = 280$ nm). The oscilloscope readings were taken at 2.5 GS/s, then sampled at 500 MS/s and filtered at 25 MHz for a) whereas the sampling and filtering were performed at 1.25 GS/s and 62.5 MHz for c). Simulated bubble growth and collapse for b) Case i and d) Case ii.

We study the bubble dynamics after the homogeneous nucleation event for two cases: i) 7.08 V applied across a $D_p = 525$ nm pore, and ii) 7.06 V applied across a $D_p = 280$ nm pore. For cases i) and ii), the initial waiting period of 16.28 µs and 12.72 µs were observed, respectively, before a bubble nucleation event. As a bubble nucleated and grew consuming the sensible heat stored around the surrounding liquid, the ion flow was blocked causing a sudden drop in the ionic current (Fig. 8a,c). We obtained the nanopore temperature distribution by the Joule heating simulations (Section

3.1) at the nucleation point observed in the experiments, $t_{\text{nuc}}$. Figure 7a,b captures the transient development of the solution temperature at the pore centre, $T_c$. We can find that at $t = t_{\text{nuc}}$, $T_c$ was around 598 K being higher than the kinetic requirement for homogeneous nucleation, 575 K (Avedisian, 1985). Thereby we confirm that the bubble homogeneously nucleated at the pore centre. In Fig. 7a,b (inset), we find that the $D_p = 525$ nm pore had a larger superheated area than that of the $D_p = 280$ nm pore at $t_{\text{nuc}}$. As a result, the nucleated bubble could grow to a larger size in the larger pore, thereby blocking the pore for a longer duration. This agrees with the experimental measurements that the blockage duration for the $D_p = 525$ nm pore was $t_b = 488$ ns and $t_b = 124$ ns for the $D_p = 280$ nm pore (Fig. 8a,c).

To theoretically capture the bubble growth dynamics during the current blockage events, we use the 1D moving boundary model (Section 3.2). Figure 8b,d reveals the time evolution of the bubble radius. For the 525 nm pore, the maximum bubble radius, $R_{\text{max}}$ reached 3066.7 nm compared to 1140.0 nm for the 280 nm pore, at $t^* = 275.99$ ns and $t^* = 90.35$ ns respectively. $t^*$ denotes the time after bubble nucleation, when the maximum radius of bubble is attained. $t_{\text{life}}$ denotes the total lifetime of the bubble. It is interesting to note that $t^*/t_{\text{life}}$ for the two cases reach 0.530 and 0.535 respectively. Additionally, when the $r$-axis and the $t$-axis are normalized by $R_{\text{max}}$ and $t_{\text{life}}$, the two curves perfectly overlap each other (Fig. 9a). This gives that the shape of $t$-$R$ curve remains nearly identical for different pore sizes. Figure 9b shows the transient variation of vapor temperature within bubbles. It is found that for the 525 nm pore a lower minimum vapor temperature was achieved than that for the 280 nm pore. As the bubbles in the 525 nm pore grew, the bubble temperature decreased to a lower level. The total lifetimes of bubbles predicted are $t_{\text{life}} = 521.20$ ns and $t_{\text{life}} = 168.84$ ns for the 525 nm and 280 nm pores, respectively. These are slightly longer than the experimental measurements, being 488 ns and 124 ns, respectively. It could because of the neglect of the heat dissipated by the pore walls in the bubble growth model (Section 3.2).
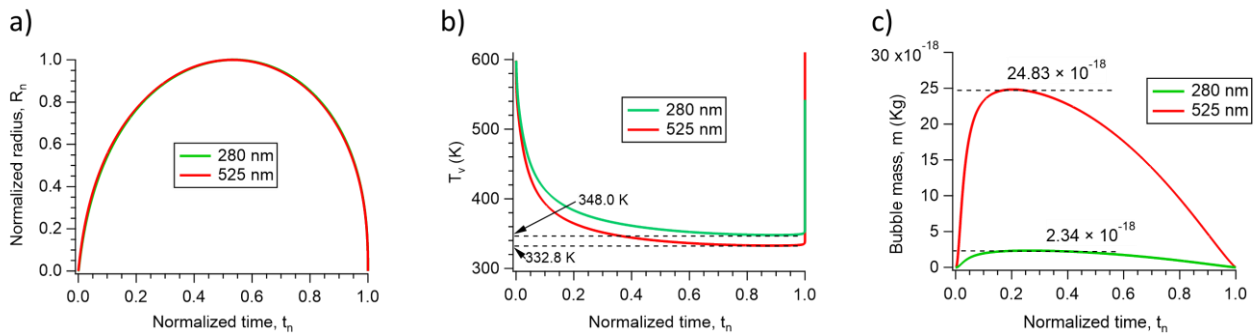


Fig. 9 Transient variations of a) the normalized bubble radius, b) the vapor temperature and c) the vapor mass inside the bubble for different pore sizes, where the $t$-axis is normalized by $t_{\text{life}}$.

The entire blockage duration can be divided into four distinct phases: i) the inertial acceleration, ii) the growth with evaporation at the interface, iii) the growth with condensation at the interface, and finally iv) the collapse with condensation at the interface. Just after the nucleation when the interface equilibrium was disturbed, the bubble interface underwent an immense acceleration of the order of $\sim 6 \times 10^{11}$ m/s$^2$ for both pore sizes (Fig. 10a). As the nucleation temperature reached ~598 K for both cases, the critical nucleus radius became ~1.5 nm according to Eq. (18). This is due to the high Laplace pressure inside the nanometer-sized critical bubble. The interface acceleration can be approximately estimated by applying the Rayleigh-Plesset equation (Eq. (15)) at $t = 0$ assuming no change in vapor pressure when $\dot{R} = 0$ m/s and $\ddot{R} = 2\gamma\Delta R/(\rho R^3) \sim 1 \times 10^{12}$ m/s$^2$, where $\Delta R \sim 0.1$ nm is the disturbance to the critical nucleus, and $\gamma$ and $\rho$ are estimated at 598 K. However, this acceleration would not last long. As the bubble volume increased, the vapor pressure would decrease according to the ideal gas law as the mass influx, $\dot{m}$ was still not enough to maintain constant vapor pressure. As the vapor pressure decreased with the growth of bubbles, the compressive surface tension force decreased as well. At $t \sim 0.5$ ns, the acceleration became zero (Fig. 10a) and interface velocity reached its maximum value (Fig. 10d). From this point onward, the Laplace pressure was higher than the vapor pressure, thus yielding a net deceleration to the bubble. This marked the end of the phase (i) and phase (ii) started.
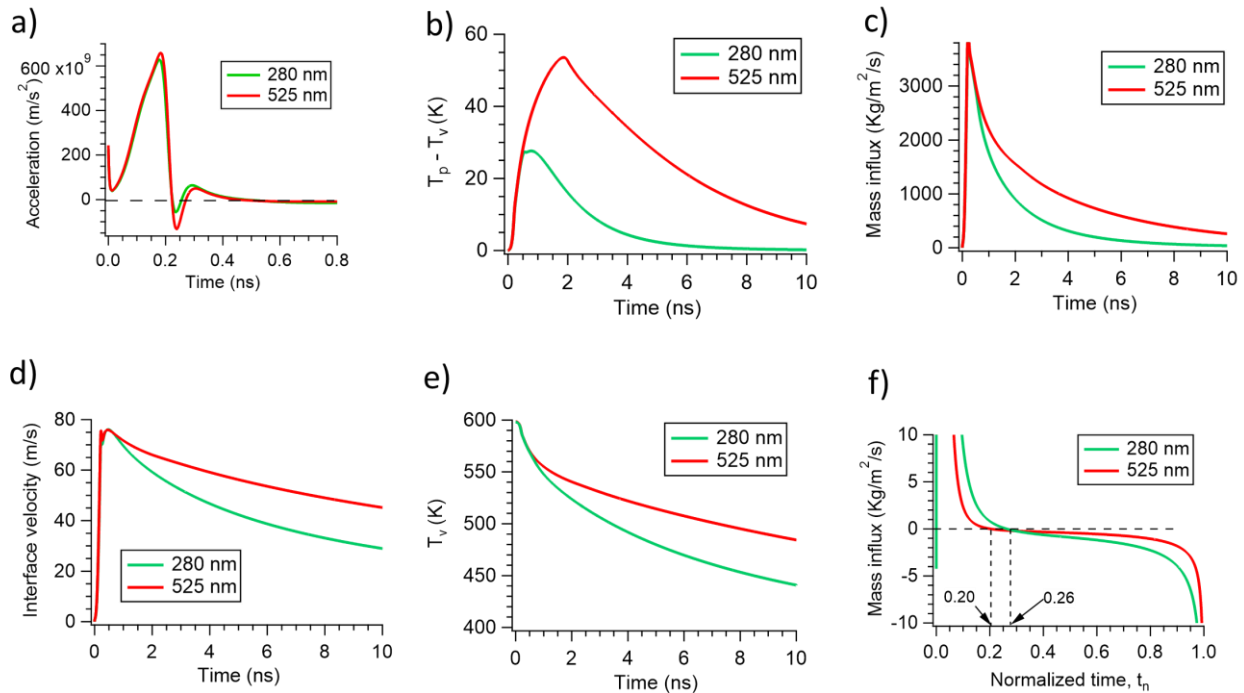
Fig. 10 Variations of the a) interface acceleration, b) interface temperature difference, c) mass influx, $\dot{m}$, d) interface velocity, e) vapor temperature with time during the initial 10ns of the bubble growth. f) Variation of $\dot{m}$ with $t_n = t/t_{\text{life}}$. The red and green curves denote the results for 525 nm and 280 nm diameter pores, respectively.

Figure 10b depicts the variation of $T_p - T_v$ with time, where $T_p$ is the peak liquid temperature across the interface thermal boundary layer and $T_v$ denotes the vapor temperature inside the bubble. As the bubble expanded, $T_v$ decreased rapidly. However, the variation of $T_p$ depended upon the shape of the temperature distribution. If the temperature distribution is flatter at the pore centre at the nucleation, $T_p$ would remain almost constant for a longer duration, resulting in a larger $T_p - T_v$. Consequently, $T_p - T_v$ was larger for the 525 nm pore (Fig. 10b) which had a flatter temperature profile than that of the 280 nm pore (Fig. 11a). As $T_p - T_v$ increased, the thermal gradient at the interface would increase, triggering the evaporation (Fig. 10c). As time progressed, the evaporative and dissipative heat fluxes, $q_r$ and $q_d$ reduced $T_p$ and $T_p - T_v$, and hence the decrease of the evaporative mass influx, $\dot{m}$ to the bubble (Fig. 10c). It is shown that the 525 nm pore had a higher $\dot{m}$, indicating the bubble pressure and temperature decreased slower than that in the 280 nm pore (Fig. 10e). Moreover, a higher vapor pressure implies a higher interface velocity for the 525 nm pore (Fig. 10d). Consequently, the 525 nm pore bubble grew to a much bigger size.

With the growth of the bubble, the mass influx continued falling. Eventually, at $t_n = 0.20$ (525 nm) and $t_n = 0.26$ (280 nm), $\dot{m} = 0$ for both cases and the condensation started at the bubble interface (Fig. 10f), marking the beginning of the phase (iii). Previously we showed that the growth of bubbles continued till $t_n \sim 0.53$. During the phase (iii), the vapor pressure decreased due to the condensation and bubble expansion, thus amplifying the interface deceleration. However due to the high initial interface velocity, bubble growth continued until $t_n = 0.53 \sim 0.54$ (the position 4, Fig. 11), where the interface velocity, $\dot{R} = 0$ and the collapse started, indicating the beginning of the phase (iv).

Figure 11 shows the radial temperature distribution inside the solution during the bubble growth and collapse for specific time points, where the bubble position 4 indicates $R_{\text{max}}$. It is interesting to note that the collapse time elapsed between the bubble positions 4 and 5 covered more than 99% of the total collapse time elapsed between the bubble positions 4 and 7. During the bubble positions 4 and 5, the bubble collapsed so slowly that the rate of collapse was primarily decided by the condensation rate and the bubble temperature remained almost constant. However, in the remaining duration of the phase (iv), the collapse rate increased because with the decrease of the bubble size, the compressive Laplace pressure increased which yielded a high shrinking acceleration. Eventually the collapse rate became extremely high that the vapor molecules inside the bubble lacked the time to escape out through the condensation and were thus intensely compressed, leading to a high vapor temperature (the bubble positions 6-7, Fig. 11). At the final bubble position, 7, when $R \sim 1.5$ nm, the vapor temperature for the 525 nm pore was much higher than its counterpart.

Compared to the 280 nm pore, the 525 nm pore had a lower bubble temperature in general during the phase (iv) (Fig. 9b), invoking a lower vapor pressure and higher surface tension. This caused a higher compressive Laplace pressure, ensuring a higher collapse acceleration. Given that the bubble mass was higher for the 525 nm pore (Fig. 9c), a high collapse rate gave rise to a steeper increase of the bubble temperature. Due to the limited bubble lifetime, it is expected that the bubble might barely contain any dissolved gas and would completely collapse into a singularity without further rebounds. After the bubble position 7, the contents inside the bubble might get ionized and emit light upon recombination, which is so-called bubble luminescence (Versluis, et al., 2000; Crum and Roy, 1994; Lohse, 2018; Supponen, et al., 2019). This marked the end of the phase (iv) and also the entire cycle of the bubble growth and collapse. As the bubble collapsed, the Joule heating resumed before the next bubble nucleation.
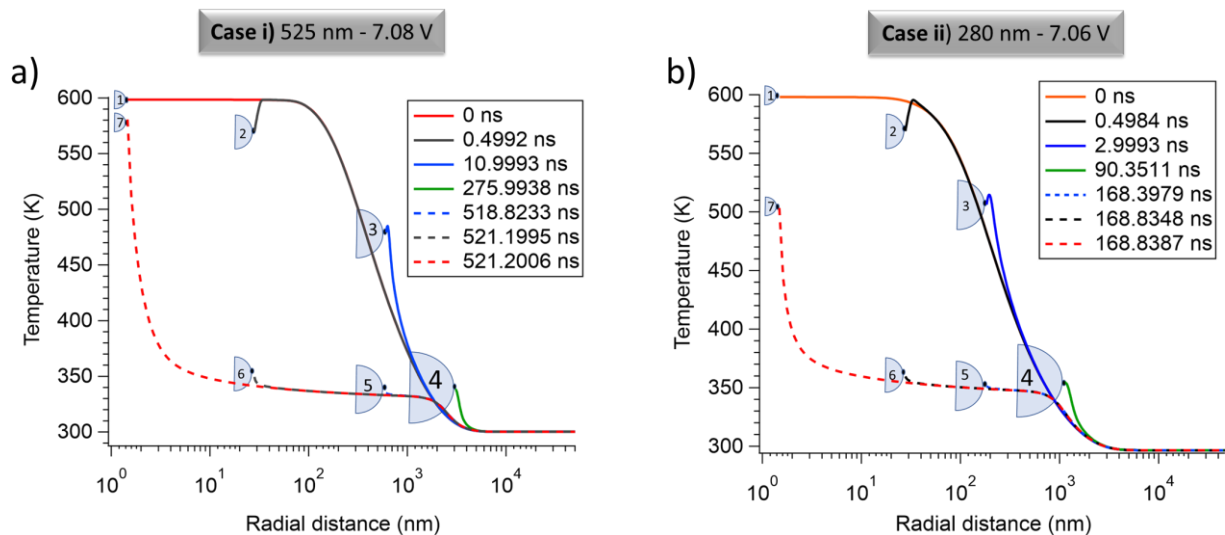


Fig. 11 Variations of the solution temperature distribution with time as the bubble grew and collapsed inside the a) 525 nm pore and b) 280 nm pore. The positions 1-4 were in the bubble growth stage while the positions 5-7 were in the collapse stage. The position 4 indicates maximum bubble size during the whole event.

## 6. Conclusion

In this article, we studied homogeneous bubble nucleation and growth in solid-state nanopore both experimentally and theoretically. Due to the focused heat generation in the nanopore, the sensible heat stored in the solution prior to nucleation was limited. Additionally, a smaller pore diameter led to a lower amount of sensible heat. As a result, the maximum bubble size and lifetime were reduced with decrease of the pore size. Using a 1D moving boundary model we successfully captured the major features of the bubble growth and collapse. The current blockage duration, due to the presence of a bubble, followed the same trend as the simulated bubble lifetime with respect to the pore size. However, the predicted bubble lifetime was slightly overestimated in the blockage duration, which may be attributed to the heat dissipation through the membrane walls neglected in the simulations. The present work will facilitate the development of a consolidated strategy for elimination of flow instabilities, from the viewpoints of rapid bubble growth at boiling incipience and vapor back flow at later stages of bubble growth, to control the nanopore nucleation and inlet restrictions. This may tremendously increase the critical heat flux limit for the next generation cooling of electronic technologies.

## Acknowledgements

## References

Ali, K. and Bilal, S., Surface tensions and thermodynamic parameters of surface formation of aqueous salt solutions: III. Aqueous solution of KCl, KBr and KI, Colloids and Surfaces A: Physicochemical and Engineering Aspects, Vol.337, No.1 (2009), pp. 194-199.

Asai, A., Application of the nucleation theory to the design of bubble jet printers, Japanese Journal of Applied Physics, Vol.28, No.5R (1989), pp. 909-915.

Avedisian, C. T., The homogeneous nucleation limits of liquids, Journal of Physical and Chemical Reference Data, Vol.14, No.3 (1985), pp. 695-729.

Brennen, C.E., Cavitation and bubble dynamics (2014), Cambridge University Press.

Chen, X., Chen, Y., Yan, M. and Qiu, M., Nanosecond photothermal effects in plasmonic nanostructures, ACS Nano, Vol.6, No.3 (2012), pp. 2550-2557.

Cooper, J.R. and Dooley, R.B., Release of the IAPWS formulation 2008 for the viscosity of ordinary water substance, The International Association for the Properties of Water and Steam (2008).

Crum, L. A. and Roy, R. A., Sonoluminescence, Physics Today, Vol.47, No.9 (1994), pp. 22-30.

Dang, B., Colgan, E., Yang, F., Schultz, M., Liu, Y., Chen, Q., Nah, J.W., Polastre, R., Gaynes, M., McVicker, G. and Parida, P., Integration and packaging of embedded radial micro-channels for 3D chip cooling. 66th Electronic Components and Technology Conference, IEEE (ECTC) (2016), pp. 1271-1277.

Debenedetti, P.G., Metastable liquids: Concepts and Principles (Vol. 1) (1996), Princeton University Press.

Gadaleta, A., Sempere, C., Gravelle, S., Siria, A., Fulcrand, R., Ybert, C. and Bocquet, L., Sub-additive ionic transport across arrays of solid-state nanopores, Physics of Fluids, Vol.26, No.1 (2014), pp. 012005.

Green, C., Kottke, P., Han, X., Woodrum, C., Sarvey, T., Asrar, P., Zhang, X., Joshi, Y., Fedorov, A., Sitaraman, S. and Bakir, M., A review of two-phase forced cooling in three-dimensional stacked electronics: technology integration. Journal of Electronic Packaging, Vol.137, No.4 (2015).

Falsetti, C., Jafarpoorchekab, H., Magnini, M., Borhani, N., and Thome, J. R., Two-phase operational maps, pressure drop, and heat transfer for flow boiling of R236fa in a micro-pin fin evaporator, International Journal of Heat and Mass Transfer, Vol.107 (2017), pp. 805-819.

Harvie, D. J. E., An implicit finite volume method for arbitrary transport equations, ANZIAM Journal, Vol.52 (2010), pp. 1126-1145.

Haynes, W. M., CRC Handbook of Chemistry and Physics (2016), CRC press.

Kandlikar, S.G. and Bapat, A.V., Evaluation of jet impingement, spray and microchannel chip cooling options for high heat flux removal, Heat Transfer Engineering, Vol.28, No.11 (2007), pp. 911-923.

Kandlikar, S.G., Kudithipudi, D. and Rubio-Jimenez, C.A., Cooling mechanisms in 3D ICs: Thermo-mechanical perspective, 2011 International Green Computing Conference and Workshops, IEEE. (2011), pp. 1-8.

Kandlikar, S. G., Colin, S., Peles, Y., Garimella, S., Pease, R. F., Brandner, J. J., and Tuckerman, D. B., Heat transfer in microchannels—2012 status and research needs, Journal of Heat Transfer, Vol.135, No.9 (2013).

Koşar, A., Kuo, C. J., & Peles, Y., Reduced pressure boiling heat transfer in rectangular microchannels with interconnected reentrant cavities, Journal of Heat Transfer, Vol.127, No.10 (2005), pp. 1106-1114.

Kuo, C.-J. and Peles, Y., Flow Boiling instabilities in microchannels and means for mitigation by reentrant cavities, Journal of Heat Transfer, Vol.130, No.7 (2008), 072402.

Levine, E. V., Burns, M. M. and Golovchenko, J. A., Nanoscale dynamics of Joule heating and bubble nucleation in a solid-state nanopore, Physical Review E, Vol.93, No.1 (2016), 13124.

Lohse, D., Bubble puzzles: From fundamentals to applications. Physical Review Fluids, Vol.3, No.11 (2018), 110504.

Madhour, Y., Olivier, J., Costa-Patry, E., Paredes, S., Michel, B., and Thome, J. R., Flow boiling of R134a in a multi-microchannel heat sink with hotspot heaters for energy-efficient microelectronic CPU cooling applications., IEEE Transactions on Components, Packaging and Manufacturing Technology, Vol.1, No.6 (2011), pp. 873-883.

Nagashima, G., Levine, E. V., Hoogerheide, D. P., Burns, M. M. and Golovchenko, J. A., Superheating and homogeneous single bubble nucleation in a solid-state nanopore, Physical Review Letters, Vol.113, No.2 (2014), pp. 24506.

Nikolayev, V. S. and Beysens, D. A., Boiling crisis and non-equilibrium drying transition. Europhysics Letters, Vol.47, No.3 (1999), pp. 345–351.

Ohmine, I. and Saito, S., Water dynamics: Fluctuation, relaxation, and chemical reactions in hydrogen bond network rearrangement, Accounts of Chemical Research, Vol.32, No.9 (1999), pp. 741-749.

Okuyama, K., Mori, S., Sawa, K. and Iida, Y., Dynamics of boiling succeeding spontaneous nucleation on a rapidly heated small surface, International Journal of Heat and Mass Transfer, Vol.49, No.15–16 (2006), pp. 2771–2780.

Park, J. Y., Peng, L., and Choi, J. W., Critical heat flux limiting the effective cooling performance of two-phase cooling with an interlayer microchannel, Microsystem Technologies, Vol.25, No.7 (2019), pp. 2831-2840.

Paul, S., Hsu, W.L., Magnini, M., Mason, L.R., Ho, Y.L., Matar, O.K. and Daiguji, H., Single-bubble dynamics in nanopores: Transition between homogeneous and heterogeneous nucleation, (2020) arXiv preprint arXiv:2007.13063.

Prajapati, Y. K. and Bhandari, P., Flow boiling instabilities in microchannels and their promising solutions – A review, Experimental Thermal and Fluid Science, Vol.88, (2017), pp. 576–593.

Prosperetti, A., Vapor bubbles, Annual Review of Fluid Mechanics, Vol.49, No.1 (2016), pp. 221–248.

Prosperetti, A. and Plesset, M. S., Vapor-bubble growth in a superheated liquid, Journal of Fluid Mechanics, Vol.85, No.2 (1978), pp. 349–368.

Robinson, A. J. and Judd, R. L., Bubble growth in uniform and spatially distrubuted temperature field, International Journal of Heat and Mass Transfer, Vol.44, No.14 (2001), pp. 2699–2710.

Robinson, A. J. and Judd, R. L., The dynamics of spherical bubble growth, International Journal of Heat and Mass Transfer, Vol.47, No.23 (2004), pp. 5101–5113.

Supponen, O., Obreschkow, D., Kobel, P., Dorsaz, N. and Farhat, M., Detailed experiments on weakly deformed cavitation bubbles, Experiments in Fluids, Vol.60, No.33 (2019).

Szczukiewicz, S., Borhani, N., and Thome, J. R., Fine-resolution two-phase flow heat transfer coefficient measurements of refrigerants in multi-microchannel evaporators, International Journal of Heat and Mass Transfer, Vol.67 (2013), pp. 913-929.

Thome, J.R. and Dupont, V., Bubble generator, U.S. Patent 7,261,144, (2007).

Versluis, M., Schmitz, B., von der Heydt, A. and Lohse, D., How snapping shrimp snap: through cavitating bubbles, Science, Vol.289, No.5487 (2000), pp. 2114-2117.

Wagner, W. and Pruß, A., The IAPWS formulation 1995 for the thermodynamic properties of ordinary water substance for general and scientific use, Journal of Physical and Chemical Reference Data, Vol.31, No.2 (2002), pp. 387-535.

Weeber, J.C., Bernardin, T., Nielsen, M.G., Hassan, K., Kaya, S., Fatome, J., Finot, C., Dereux, A. and Pleros, N., Nanosecond thermo-optical dynamics of polymer loaded plasmonic waveguides, Optics Express, Vol.21, No.22 (2013), pp. 27291-27305.

Xu, J., Liu, G., Zhang, W., Li, Q. and Wang, B., Seed bubbles stabilize flow and heat transfer in parallel microchannels, International Journal of Multiphase Flow, Vol.35, No.8 (2009), pp. 773–790.

Yin, L., Jiang, P., Xu, R., Hu, H. and Jia, L., Heat transfer and pressure drop characteristics of water flow boiling in open microchannels, International Journal of Heat and Mass Transfer, Vol.137 (2019), pp. 204-215.

Yun, R., Kim, Y., and Kim, M. S., Convective boiling heat transfer characteristics of CO2 in microchannels. International Journal of Heat and Mass Transfer, Vol.48, No.2 (2005), pp. 235-242.